CONDENSED MATTER PHYSICS

Suppression of antiferromagnetic order by strain-enhanced frustration in honeycomb cobaltate

Gye-Hyeon Kim[1]†, Miju Park[1]†, Subhasis Samanta[2,3]†, Uksam Choi[1], Baekjune Kang[1], Uihyeon Seo[1], GwangCheol Ji[4], Seunghyeon Noh[5], Deok-Yong Cho[6], Jung-Woo Yoo[5], Jong Mok Ok[4], Heung-Sik Kim[2]*, Changhee Sohn[1]*

Layered honeycomb cobaltates are predicted as promising for realizing the Kitaev quantum spin liquid, a many-body quantum entangled ground state characterized by fractional excitations. However, they exhibit antiferromagnetic ordering at low temperatures, hindering the expected quantum state. We demonstrate that controlling the trigonal distortion of CoO_6 octahedra is crucial to suppress antiferromagnetic order through enhancing frustration in layered honeycomb cobaltates. Using heterostructure engineering on $Cu_3Co_2SbO_6$ thin films, we adjust the trigonal distortion of CoO_6 octahedra and the resulting trigonal crystal field. The original Néel temperature of 16 kelvin in bulk $Cu_3Co_2SbO_6$ decreases (increases) to 7.8 kelvin (22.7 kelvin) in strained $Cu_3Co_2SbO_6$ films by decreasing (increasing) the magnitude of the trigonal crystal fields. The first-principles calculation suggests the enhancement of geometrical frustration as the origin of the suppression of antiferromagnetism. This finding supports the potential of layered honeycomb cobaltate heterostructures and strain engineering in realizing extremely elusive quantum phases of matter.

INTRODUCTION

The small amount of broken local symmetry has been blamed for making a whole many-body quantum entangled state collapse into a (quasi)classical product state. Ever since Anderson's idea of resonating valence bond (1, 2), searching for many-body quantum entangled ground states and low-energy excitation in the matter has remained an important but highly elusive task in condensed matter physics (3, 4). An outstanding example is the Kitaev quantum spin liquid (QSL), in which bond-dependent Ising interactions of spins on a two-dimensional honeycomb lattice induce macroscopic quantum entanglement and fractional excitations (5). While intensive studies have found signatures of fractionalization in candidate materials such as Na_2IrO_3 (6–10) and α-$RuCl_3$ (11–17), all of them have shown classical long-range antiferromagnetic orderings at sufficiently low temperatures. The convincing hypotheses about the collapse of the predicted quantum state in low temperatures have pointed out broken local symmetry as a culprit (8, 16). For example, finite trigonal distortions act as one of the main effects in generating non-Kitaev spin interactions in various candidate materials (16, 18, 19), deviating from the original concept of realizing Kitaev QSL through edge-shared cubic octahedra as shown in Fig. 1A (20). Therefore, experimental verification of strong correlations between local distortions and stability of classical ground states would mark a prominent milestone in realizing these notoriously elusive quantum phases of matter.

In this context, $Cu_3Co_2SbO_6$, a layered honeycomb cobaltate, can be an exemplary model system for probing the hypothesized relationship between local trigonal distortion and magnetic ground state. Theoretical (18, 21, 22) studies suggested that layered honeycomb cobaltate can be in close vicinity of Kitaev QSL as their orbital structures can be described as spin-orbit entangled $J_{eff} = 1/2$ states (22); the subsequent experiments (23–29) have also shown frustration in spin exchange interaction (25, 29) and the presence of fractionalized particle in the system (27, 28) as the evidences of the proximity to QSL phases. However, because of the relatively small spin-orbit coupling strength of Co^{2+} ions, the presence of compressive trigonal distortion is expected to break $J_{eff} = 1/2$ orbital pictures rather easily, favoring the stabilization of a single a_{1g} and doubly degenerate e_g^π orbitals (Fig. 1A) (30). Therefore, previous theoretical studies suggested that the Kitaev QSL state could be realized only with a small trigonal distortion in the layered honeycomb cobaltates (22). As shown in Fig. 1B, $Cu_3Co_2SbO_6$ has distorted local octahedra and displays classical antiferromagnetic ordering near 16 K (31) consistent with the aforementioned theoretical hypotheses. Notably, unlike other Kitaev material candidates, this compound has been successfully synthesized in thin film (32), facilitating the application of lattice engineering, which enables manipulation of local distortion of CoO_6 octahedra (33–35).

Here, we present the control of the local trigonal distortion induces a wide modulation in the Néel temperature (T_N) of $Cu_3Co_2SbO_6$. By using $Cu_3Co_2SbO_6$ (001) film grown on ZnO (0001) substrate (32), we successfully manipulated the trigonal distortion of the CoO_6 octahedra (Fig. 1C). We observed that the ultrathin $Cu_3Co_2SbO_6$ film got strained on the ZnO substrate, notwithstanding the large lattice mismatch (+4.3%). This strain allowed us to stretch the octahedra in the in-plane direction, resulting in an increased compressive trigonal distortion. Because of the absence of a suitable substrate for out-of-plane stretching in the octahedra, we conducted helium implantation on the bulk-like 20–unit cell (u.c.) $Cu_3Co_2SbO_6$ films. This is a well-known methodology for out-of-plane expansion of CoO_6 octahedra, thereby mitigating the compressive trigonal distortion (35). X-ray

[1]Department of Physics, Ulsan National Institute of Science and Technology, Ulsan 44919, Republic of Korea. [2]Department of Semiconductor Physics and Institute of Quantum Convergence Technology, Kangwon National University, Chuncheon 24341, Republic of Korea. [3]Center for Extreme Quantum Matter and Functionality, Sungkyunkwan University, Suwon 16419 Republic of Korea. [4]Department of Physics, Pusan National University, Busan 46241, Republic of Korea. [5]Department of Materials Science and Engineering, Ulsan National Institute of Science and Technology, Ulsan 44919, Republic of Korea. [6]Department of Physics, Jeonbuk National University, Jeonju 54896, Republic of Korea.
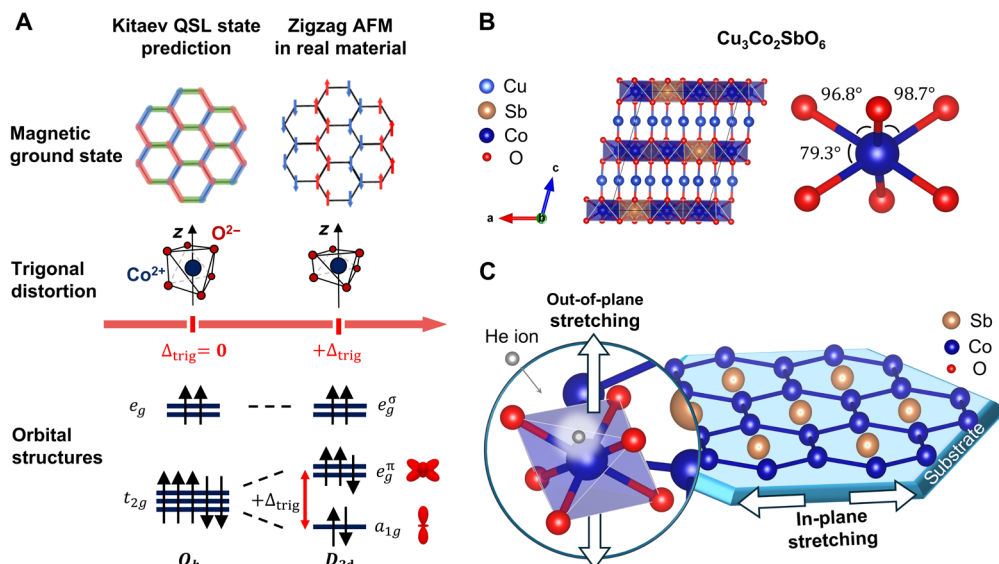*Corresponding author. Email: chsohn@unist.ac.kr (C.S.); heungsikim@kangwon.ac.kr (H.-S.K.)
†These authors contributed equally to this work.

Fig. 1. Strain engineering of local trigonal distortion of CoO6 octahedra in layered honeycomb cobaltate Cu3Co2SbO6. (**A**) Relationship among local trigonal distortion of CoO6 octahedra, orbital structures, and the magnetic ground state of Cu3Co2SbO6. The t_{2g} orbitals in the O_h system split into e_g^π orbitals and a_{1g} orbital by trigonal distortion of CoO6 octahedra with D_{3d} symmetry. The energy difference between the e_g^π and a_{1g} level is defined by the Δ_{trig}. According to theoretical predictions, the Kitaev QSL state could be realized with decreasing Δ_{trig} in the layered honeycomb cobaltates. (**B**) The crystal structure of layered honeycomb cobaltate Cu3Co2SbO6 and O—Co—O bond angles of CoO6 octahedra, indicating compressed octahedra along the out-of-plane direction [z axis in (A)]. (**C**) Two ways for modulating Δ_{trig} of CoO6 octahedra. While helium implantation would decrease Δ_{trig} by stretching the octahedra along the out-of-plane direction, the strain imposed on the ultrathin film through the substrate would increase Δ_{trig} by stretching the octahedra in the in-plane direction.

absorption spectroscopy (XAS) combined with crystal field multiplet calculations reveals a clear increase (decrease) of trigonal crystal field Δ_{trig} of CoO6 octahedra by reducing film thickness (by helium implantation), indicating successful control of trigonal distortions. Consequently, the original T_N of 16 K in Cu3Co2SbO6 was modulated from 22.7 to 7.8 K, depending on the direction and the magnitude of the applied stretching. The transition temperature T_N can be increased by up to one and a half times or decreased by half via the structural tuning, indicating a strong correlation between trigonal distortion and the stability of classical antiferromagnetic ground states. The first-principles calculation further elucidates how trigonal distortion control effectively modulates the various spin exchange interactions and enhances frustration in this compound. Our findings suggest the possible way to enhance the frustration in spin exchange interactions by strain, which might guide the honeycomb cobaltates to potential spin liquid phases.

RESULTS
Orbital structure of Co²⁺ ion in honeycomb cobaltates
We first compare Co L-edge XAS of bulk-like 20-u.c. Cu3Co2SbO6 film with that of Na3Co2SbO6 film to elucidate the rather controversial relationship between orbital structures and distorted local CoO6 octahedra in layered honeycomb cobaltates. Note that Na3Co2SbO6 has an almost identical local structure of CoO6 octahedra to Cu3Co2SbO6, except for its smaller trigonal distortion (fig. S1). Considering crystal fields only from O²⁻ ions, we can expect positive Δ_{trig} with a lower energy of a_{1g} orbitals than that of e_g^π orbitals in both compounds (Fig. 2A), as the octahedra are compressed in the out-of-plane direction (Fig. 1A). However, previous theoretical and experimental research on Na3Co2SbO6 suggested the negative value of Δ_{trig} (22, 36). It has been attributed that the size of the negative crystal field from Sb⁵⁺ ions is larger than the size of the positive crystal field from O²⁻ ions (Fig. 2A).

Despite those predictions for Δ_{trig}, the Cu3Co2SbO6 displayed a notably larger x-ray linear dichroism (XLD) in Co L_3-edge spectra than Na3Co2SbO6, implying a more dominant role of O²⁻ than Sb⁵⁺ ions in Δ_{trig} and the positive sign in total Δ_{trig}. Figure 2 (B and C) exhibits the normalized isotropic XAS, $I_{iso} = (2I_{\perp z} + I_{\parallel z})/3$, and XLD, $I_{XLD} = I_{\perp z} - I_{\parallel z}$, at the Co L_3 edges for Cu3Co2SbO6 and Na3Co2SbO6, respectively. Here, $I_{\perp z}$ ($I_{\parallel z}$) denotes the XAS spectra with the incident polarization (denoted as **E**) of light perpendicular (parallel) to the out-of-plane direction. We changed the polarization of the incident x-ray with a fixed incident angle α of 70° with respect to the surface normal vector (20° between the incident wave vector of x-ray and the sample surface) (fig. S2). From this experimental geometry, the spectra for the polarization were obtained by using the formula, $I_{\perp z} = I_p$ and $I_{\parallel z} = [I_s - I_p\cos^2(\alpha)]/\sin^2(\alpha)$, where I_p (I_s) are the measured intensities with p (s) polarization. The I_{iso} spectra at the Co L_3 edge of both compounds are nearly identical and resemble the well-known spectra of Co²⁺ ions (37). The major difference in those spectra is that the I_{XLD} of Cu3Co2SbO6 is roughly two times larger than that of Na3Co2SbO6, indicating a larger magnitude of Δ_{trig} (38). This result contrasts with the previous theoretical predictions, which suggested a dominant Sb⁵⁺ crystal field and a negative Δ_{trig}. If Δ_{trig} were negative in layered honeycomb cobaltates, then a more distortion in octahedra in Cu3Co2SbO6 than Na3Co2SbO6 would reduce the overall magnitude of Δ_{trig} with a larger positive crystal field from O²⁻. The comparison between these two similar compounds underlines the dominant influence of the O²⁻ crystal field and supports a positive Δ_{trig} in layered honeycomb cobaltates (Fig. 2A).
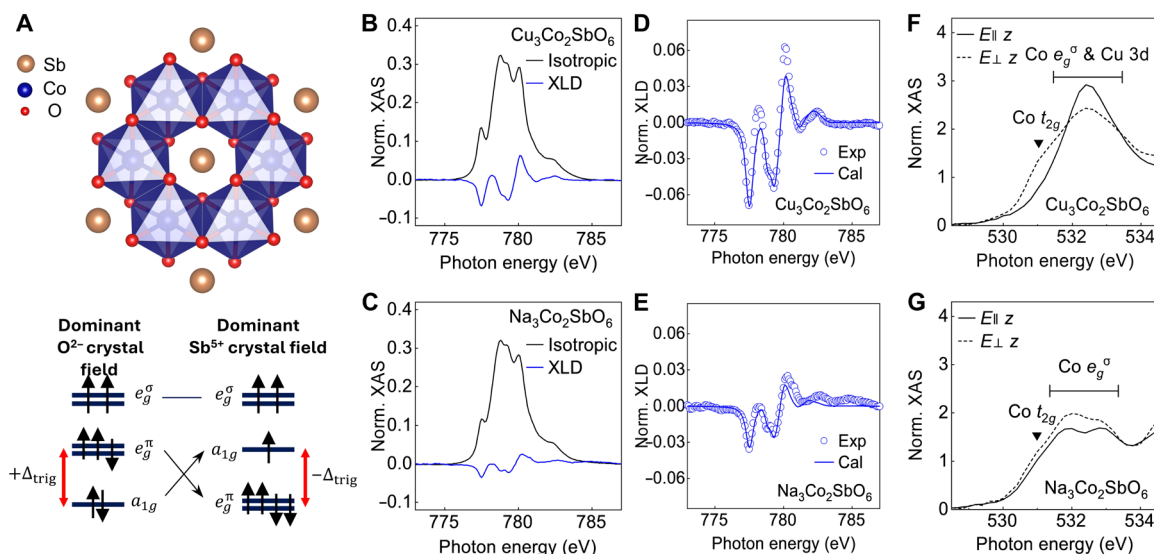
Fig. 2. Trigonal crystal field and orbital structure of Co^{2+} ion in Cu$_3$Co$_2$SbO$_6$ and Na$_3$Co$_2$SbO$_6$. (**A**) Top view of layered honeycomb cobaltates with triangular Sb^{5+} lattice (top) and orbital structures of Co^{2+} ion with respect to trigonal crystal field Δ_{trig} (bottom). The orbital structures of Co^{2+} ions are influenced by both Sb^{5+} and O^{2-} crystal fields, with the total Δ_{trig} sign determined by the dominant crystal field between Sb^{5+} and O^{2-} ions, which have opposite charges. Isotropic XAS, $I_{\text{iso}} = (2I_{\perp z} + I_{\parallel z})/3$, and XLD, $I_{\text{XLD}} = I_{\perp z} - I_{\parallel z}$, of Co L_3 edge in (**B**) Cu$_3$Co$_2$SbO$_6$ and (**C**) Na$_3$Co$_2$SbO$_6$. $I_{\perp z}$ ($I_{\parallel z}$) is normalized XAS signals with each polarization, **E** field perpendicular (parallel) to the out-of-plane direction. The experimental XLD data (open circles) and the simulation from crystal field multiplet calculation (solid lines) of (**D**) Cu$_3$Co$_2$SbO$_6$ and (**E**) Na$_3$Co$_2$SbO$_6$. On the basis of calculations within trigonal symmetry, the trigonal field strength is deduced to be 37.8 and 25.1 meV for Cu$_3$Co$_2$SbO$_6$ and Na$_3$Co$_2$SbO$_6$, respectively. The polarization-dependent O K-edge XAS for (**F**) Cu$_3$Co$_2$SbO$_6$ and (**G**) Na$_3$Co$_2$SbO$_6$. Individual peaks can be assigned to unoccupied O 2p orbitals hybridized with Co 3d t_{2g} and e_g orbitals. In Cu$_3$Co$_2$SbO$_6$, the additional peak near 532.5 eV is the known transition from O 1s to O 2p–Cu 3d hybridized state in Cu$^+$ valence systems. In both compounds, the intensity of the Co t_{2g} peak is enhanced in $I_{\perp z}$, indicating dominant e_g^π symmetry in the unoccupied state of the Co^{2+} ion.

For estimating the magnitude of Δ_{trig}, the crystal field multiplet calculations were conducted using the quantum many-body script language, Quanty (*39*) with Crispy interface (*40*). This multiplet calculation includes atomic parameters, such as Slater-Condon parameter and spin-orbit coupling constant, and crystal field parameters, including octahedral field parameter Dq and trigonal parameters D_σ and D_τ. The crystal field parameters are mainly influenced by the geometry of our trigonally distorted CoO$_6$ octahedra system. The crystal field parameters, D_σ, D_τ, and Dq, were determined by fitting the experimental I_{XLD} with the calculated spectra. These parameters can be used to obtain Δ_{trig} by diagonalizing the crystal field Hamiltonian (see Materials and Methods and the Supplementary Materials). The best fitting parameters for I_{XLD} of Cu$_3$Co$_2$SbO$_6$ (Na$_3$Co$_2$SbO$_6$) film result in $\Delta_{\text{trig}} = 37.8$ meV (25.1 meV). This multiplet calculation is consistent with the above qualitative analysis.

The polarization-dependent O K-edge spectra further clarify unoccupied e_g^π orbitals and positive Δ_{trig} in the layered honeycomb cobaltates. The Co^{2+} ions in layered honeycomb cobaltates exhibit high spin d^7 configurations. Therefore, in O K-edge XAS of Cu$_3$Co$_2$SbO$_6$ and Na$_3$Co$_2$SbO$_6$ (Fig. 2, F to G), the lowest energy peak near 531 eV can be assigned to O 2p–Co t_{2g} hybridized state, while the multiple-peak features at higher energies are associated with O 2p orbitals hybridized with unoccupied Co e_g^σ and Cu 3d orbitals (fig. S3) (*41–45*). Given that trigonal distortion splits only the t_{2g} orbitals, we focused on polarization dependence in the lowest peak. In the O K edge, $I_{\perp z}$ ($I_{\parallel z}$) of the peak is proportional to the averaged interatomic matrix element V_{pd}^2 between Co t_{2g} orbitals and O 2p orbitals perpendicular (parallel) to the out-of-plane direction. Consequently, the relative intensity between $I_{\perp z}$ and $I_{\parallel z}$ is sensitive to

whether the orbital character of the unoccupied t_{2g} orbital is mainly a_{1g} or e_g^π. The intensity ratio, $I_{\perp z}/I_{\parallel z}$, for the a_{1g} orbital character is calculated to be 0.25 in undistorted cubic octahedra and is expected to be less than 0.25 in the presence of trigonal distortions. That for e_g^π symmetry, on the other hand, is expected to be 1 in undistorted cubic octahedra and larger than 1 with trigonal distortion (*44*). Therefore, if those cobaltates had a negative Δ_{trig} and unoccupied a_{1g} orbitals as predicted, then we would observe a strong suppression in Co t_{2g} peak intensity in $I_{\perp z}$ compared to $I_{\parallel z}$ spectra. However, both compounds show enhancement of the peak intensity in $I_{\perp z}$ than in $I_{\parallel z}$, unambiguously indicating that the unoccupied e_g^π orbitals are dominant and that Δ_{trig} is positive.

Strain engineering in Cu$_3$Co$_2$SbO$_6$ heterostructure

By using our heterostructure geometry, we have successfully controlled the crystal structure and trigonal distortion of Cu$_3$Co$_2$SbO$_6$ thin films. Figure 3A exhibits x-ray diffraction (XRD) θ-2θ scan near the (008) peak of Cu$_3$Co$_2$SbO$_6$ film with 20-u.c. and 3-u.c. thickness. The (008) peak of 3-u.c. Cu$_3$Co$_2$SbO$_6$ film shifts to a higher angle than that of 20-u.c. Cu$_3$Co$_2$SbO$_6$ film, indicating reduced out-of-plane lattice constant, c^* [$c^* = c\sin(\beta)$ in lattice parameter] with thickness (*33*). As shown in Fig. 3B, c^* is quickly relaxed to its bulk value with increasing thickness due to the large lattice mismatch (+4.3%) between ZnO and Cu$_3$Co$_2$SbO$_6$ (fig. S4). Reciprocal space mapping (RSM) data and q_x profiles (Fig. 3, C and D) of the Cu$_3$Co$_2$SbO$_6$ (606) plane further demonstrate that the q_x value for the 3-u.c. film is smaller than that of the 20-u.c. film, indicative of an in-plane elongation. On the basis of these findings, we conclude that, despite the notable lattice mismatch, a tensile strain is imparted
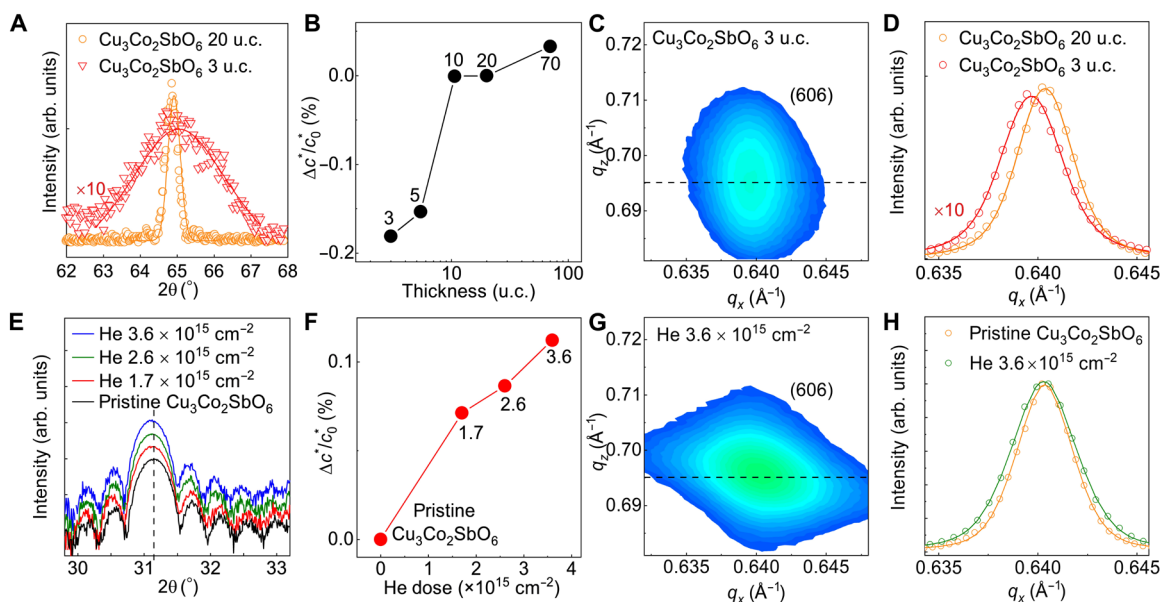
Fig. 3. Strain engineering in $Cu_3Co_2SbO_6$ heterostructure. (**A**) XRD θ-2θ scan of near the $Cu_3Co_2SbO_6$ (008) peak of 3-u.c. and 20-u.c. film in linear scale. The tensile strain from the ZnO substrate induced expansion of the out-of-plane lattice parameter, resulting in a shift of the (008) peak of $Cu_3Co_2SbO_6$ to a higher angle. (**B**) The change of out-of-plane lattice parameter, $\Delta c^*/c^*_0$ as a function of thickness in $Cu_3Co_2SbO_6$ thin film. Δc^* was calculated with respect to c^* of 20-u.c. film, c^*_0. Because of the huge lattice mismatch between ZnO and $Cu_3Co_2SbO_6$, the tensile strain rapidly relaxed as the thickness of the film increased. (**C**) Reciprocal space mapping (RSM) and (**D**) q_x profile for (606) plane of 3-u.c. $Cu_3Co_2SbO_6$ thin film. A smaller q_x value in 3-u.c. thin film than that in 20-u.c. thick film indicates the in-plane stretching in ultrathin film (fig. S5). (**E**) XRD θ-2θ scan and (**F**) $\Delta c^*/c^*_0$ of $Cu_3Co_2SbO_6$ film as a function of doses of helium ion. The (004) peak of $Cu_3Co_2SbO_6$ shifts to lower angles with increased dosed helium ions, indicating out-of-plane stretching of the lattice. (**G**) RSM image and (**H**) q_x profile of the He-implanted $Cu_3Co_2SbO_6$ thin film (3.6×10^{15} cm^{-2}; fig. S5). The peak from helium-implanted film maintains the same q_x position as that of the pristine 20-u.c. film due to its epitaxially locked in-plane lattice constants.

upon the ultrathin $Cu_3Co_2SbO_6$ films. To increase c^*, on the other hand, we adopted helium implantation as helium atoms in matter induce c^* expansion with epitaxially locked in-plane lattice constants (*34*, *35*). For helium implantation, the bulk-like 20-u.c. $Cu_3Co_2SbO_6$ films were used. As we increased the dose of helium ions, the (004) peak of $Cu_3Co_2SbO_6$ films shifted to a lower angle, consistent with increased c^* (Fig. 3, E and F). Same as thickness-controlled films, we obtained RSM and q_x profiles of the $Cu_3Co_2SbO_6$ (606) plane for the He-implanted film (3.6×10^{15} cm^{-2}) (Fig. 3, G and H). As we expected, helium implantation barely modulates in-plane lattice constant compared to pristine $Cu_3Co_2SbO_6$ due to its locked lattice by neighboring unit cells. Full RSM images for each sample are shown in fig. S5. It is noteworthy that inhomogeneity of strain in thicker $Cu_3Co_2SbO_6$ layers, even with helium implantation, was found to be negligible as shown in the annular dark-field scanning transmission electron microscopy (ADF-STEM) images and the strain mapping by conducting geometrical phase analysis (fig. S6).

The observed decrease (increase) of c^* in $Cu_3Co_2SbO_6$ films enhances (suppresses) the trigonal distortion of the octahedra and Δ_{trig}. Figure 4A exhibits the evolution of I_{XLD} of Co L_3 edge with thickness and helium implantation. I_{XLD} of 3-u.c. $Cu_3Co_2SbO_6$ film shows an overall enhancement compared to the 20-u.c. $Cu_3Co_2SbO_6$ film, indicating an increased Δ_{trig} (Fig. 4A, left). The He-implanted $Cu_3Co_2SbO_6$ films (3.6×10^{15} cm^{-2}), in contrast, exhibit smaller I_{XLD} relative to the pristine $Cu_3Co_2SbO_6$ film (Fig. 4A, right), indicating a decreased Δ_{trig}. Figure 4B shows the absolute area of XLD, $I_{|XLD|}$, in each stretched-thin film, which roughly represents the relative magnitude of Δ_{trig} (*38*), as well as simulated Δ_{trig}, which reproduced experimental I_{XLD} (fig. S7). Notably, $I_{|XLD|}$ of both

the 3-u.c. film and the He-implanted film (3.6×10^{15} cm^{-2}) are increased (reduced) to ~13% (33%) of the original value in the bulk-like $Cu_3Co_2SbO_6$, demonstrating capabilities of heterostructures for the direct control of Hamiltonian parameters.

Modulation of the Néel temperature induced by strain engineering

To investigate the effect of the trigonal distortion and Δ_{trig} on its magnetic ground state, we conducted spectroscopic ellipsometry to detect T_N in strained $Cu_3Co_2SbO_6$ films. The previous research on $Cu_3Co_2SbO_6$ has shown a peculiar spin-exciton coupling that induces a distinct kink at T_N in a raw ellipsometric parameter Ψ, here tanΨ is the intensity ratio between reflected p- and s-polarized light at the exciton peak energy of ~4 eV (fig. S8). Therefore, we fixed the photon energy at the resonant frequency of the exciton and obtained temperature-dependent Ψ as shown in Fig. 5 (A to F). Note that conventional magnetometry experiments make it difficult to detect T_N of ultrathin film owing to its extremely small volume and large paramagnetic/diamagnetic backgrounds from substrates, defects, and equipment environment (fig. S9). This optical detection of T_N is not only sufficiently sensitive for ultrathin films but also free from any paramagnetic and diamagnetic backgrounds as no external magnetic field is required. Figure 5A shows Ψ (*T*) of 20-u.c. $Cu_3Co_2SbO_6$ thin film. Even without complicated model fitting, we observed a clear kink at ~16 K in the raw ellipsometry parameter, which is consistent with T_N observed in conventional magnetometry experiments.

The strain engineering on $Cu_3Co_2SbO_6$ films and the resultant change in Δ_{trig} induced a massive modulation in T_N. Figure 5 (A to F) exhibits optical parameter Ψ of strained $Cu_3Co_2SbO_6$ thin films as a
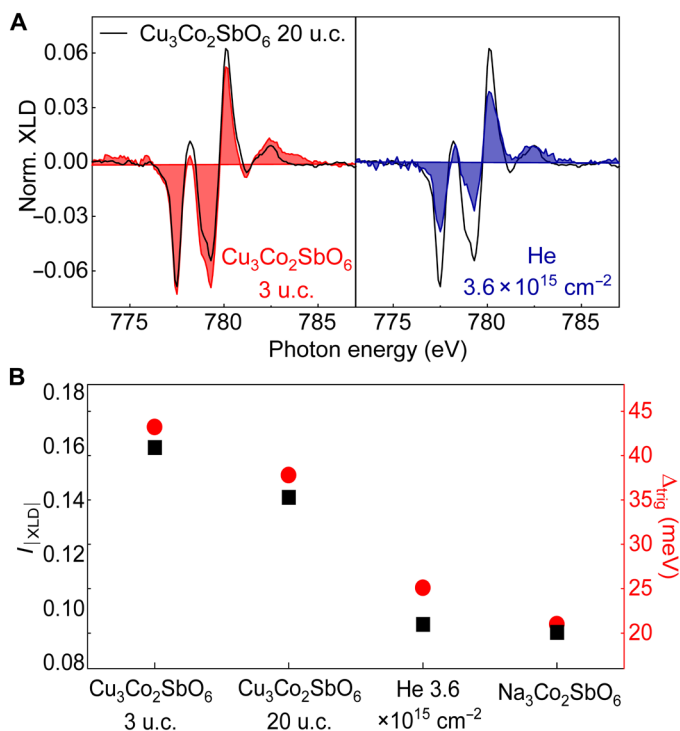
Fig. 4. Strain control of Δ_{trig} in $Cu_3Co_2SbO_6$ thin films. (**A**) I_{XLD} of Co L_3 edge for 3-u.c. $Cu_3Co_2SbO_6$ thin film (left) and He-implanted $Cu_3Co_2SbO_6$ thin film (3.6 × 10^{15} cm^{-2}; right). For comparison, I_{XLD} of 20-u.c. $Cu_3Co_2SbO_6$ is also shown as black lines. Films with more out-of-plane stretching showed decreased XLD signals, while films with increased in-plane stretching showed larger XLD signals. This observation clearly indicates the successful modulation of the Δ_{trig}. (**B**) The absolute area of XLD, $I_{|XLD|}$, and Δ_{trig} deduced from the crystal field multiplet calculation of XLD spectra for 3-u.c. $Cu_3Co_2SbO_6$ film, 20-u.c. $Cu_3Co_2SbO_6$ film, He-implanted $Cu_3Co_2SbO_6$ film (3.6 × 10^{15} cm^{-2}), and $Na_3Co_2SbO_6$ film.

function of T. While T_N of the 3-u.c. $Cu_3Co_2SbO_6$ film with a larger Δ_{trig} is shifted to 22.7 ± 1.8 K (Fig. 5C), T_N in the He $Cu_3Co_2SbO_6$ films (3.6 × 10^{15} cm^{-2}) with a reduced Δ_{trig} is suppressed to 7.8 ± 1 K (Fig. 5F). Note that the observed increased T_N in ultrathin film is not from dimensional effect but from strain, as fully relaxed and ultrathin film on $MgAl_2O_4$ substrate shows negligible change in T_N (fig. S10). In addition, the reduced T_N in helium-implanted films can hardly be attributed to any extrinsic origins such as impurity formation, as it recovered to the original value of 16 K with the removal of the helium ions through mild thermal annealing (fig. S11) (35). Figure 5G is a summary of our discovery of strong positive correlations between Δ_{trig} and T_N in layered honeycomb cobaltates. Although the $Na_3Co_2SbO_6$ has a different space group ($C\,2/m$) (46) compared to $Cu_3Co_2SbO_6$ ($C\,2/c$) (31), it follows the same relationship between Δ_{trig} and T_N observed in $Cu_3Co_2SbO_6$ films, as highlighted by a star in Fig. 5G. It is strong evidence that reducing trigonal distortion in CoO_6 octahedra is a key to destabilizing classical ground states in layered honeycomb cobaltates.

## First-principles calculation on strained $Cu_3Co_2SbO_6$

We performed first-principles calculation to elucidate how strain modulates various exchange interactions and thereby suppresses the long-range ordering in $Cu_3Co_2SbO_6$. Early theoretical studies on layered honeycomb cobaltates claimed that reduced trigonal distortion can suppress Heisenberg and other exchange interactions except the Kitaev term (18, 21, 22). However, recent theoretical and experimental results suggest the existence of several other exchange paths, which could lead the system more closer to the XXZ spin model with geometrical frustration between the nearest-neighbor Heisenberg interaction J_1 and third nearest-neighbor interaction J_3 (47–50). Therefore, the detailed mechanism of the observed correlations between trigonal distortion and T_N could be more complicated than the naïve expectation. In this regard, we performed first-principles electronic structure calculations to elucidate how strain-induced trigonal distortion modulates various exchange interactions and thereby suppresses the long-range ordering in $Cu_3Co_2SbO_6$. First, we optimized crystal structures under the controlled strain. Spin Hamiltonians under stain were computed by using a fourth-order strong coupling perturbation theory afterward (50). The details of calculation methods, relevant hopping parameters, and exchange interactions of each strained case are shown in Materials and Methods and the Supplementary Materials.

The first-principles structural optimization shows that the trigonal distortion is the major structural change by experimental lattice stretching for both the in-plane and out-of-plane directions, consistent with our expectation. To simulate the out-of-plane stretching condition by helium implantation, we fixed the in-plane lattice parameter while stretching the system along the c axis (left side of Fig. 6A). For the case of in-plane stretching (right side of Fig. 6A), on the other hand, we control the in-plane lattice parameters and allow the lattice vector along the out-of-direction to relax accordingly. As a result, Co—Co bond length is changed only for the case of in-plane stretching, consistent with our experimental observation. With this asymmetric condition, the trigonal distortion angle, defined as the average of O—Co—O angle, $\varphi = (\varphi_1 + \varphi_2 + \varphi_3)/3$, is almost linearly increased with strain, thereby proving our strain controls manipulated the trigonal distortion and resulting Δ_{trig}. Note that other structural distortions such as rotational distortion were found to be negligible in this calculation.

In the ambient condition, the strong-coupling perturbation theory reveals that the three leading terms in spin Hamiltonian are the nearest-neighbor ferromagnetic Kitaev term K_1 (−2.207 meV), ferromagnetic J_1 (−1.04 meV), and antiferromagnetic J_3 (1.664 meV), as depicted in Fig. 6B. It suggests that the spin Hamiltonian of $Cu_3Co_2SbO_6$ can be understood as a Heisenberg-Kitaev model with a prominent third nearest-neighbor J_3 (51). The comparable energy scales among the three terms indicate the presence of the geometrical frustration between J_1 and J_3, in addition to the exchange frustration induced by K_1.

We found that the decrease in trigonal distortion causes the enhancement of the ferromagnetic J_1 exchange interaction, resulting in stronger geometrical frustration and destabilization of the zigzag antiferromagnetic ordering. Figure 6C displays the evolution of J_1, J_3, and K_1 as we stretch $Cu_3Co_2SbO_6$ in the in-plane and out-of-plane directions. While J_3 is weakly affected by the strain, J_1 shows an almost linear relationship with the trigonal distortion: The magnitude of J_1 increases (decrease) with the decrease (increase) of trigonal distortion. This tendency is mainly caused by the change of the direct overlap process between nearest-neighboring t_{2g} orbitals (the t_3 term in table S1; see the relevant section in the Supplementary Materials for further details) via the Co—O—Co bond angle change involved in the trigonal distortion.
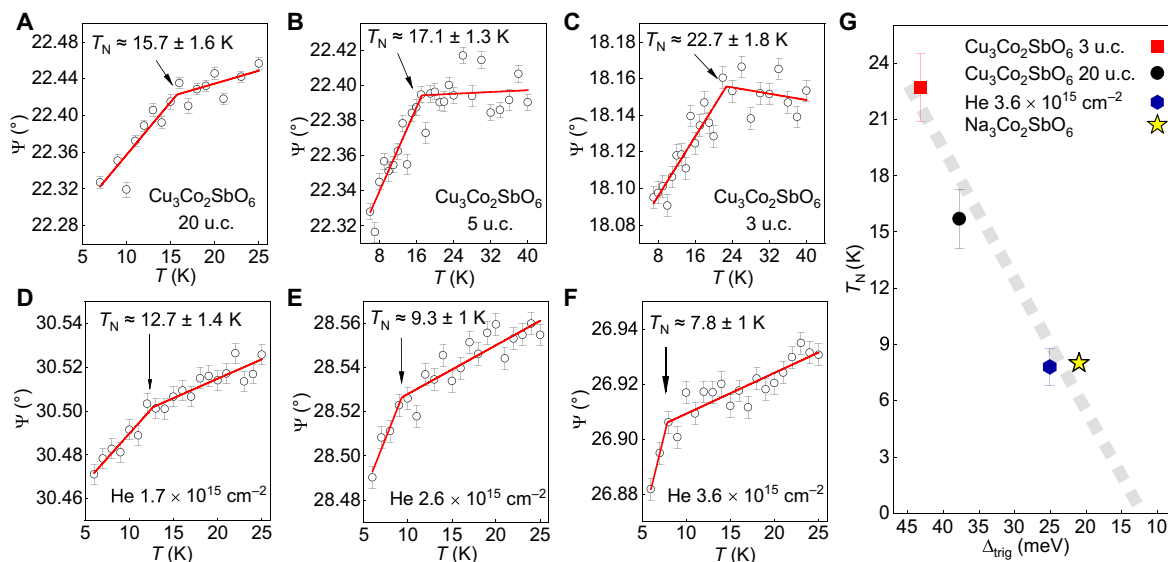
Fig. 5. Wide modulation of T_N induced by strain engineering in $Cu_3Co_2SbO_6$. The T-dependent ellipsometric parameter Ψ (open circles) at exciton peak energies, which can be used to detect T_N via spin-exciton coupling: The red solid lines are piecewise function fitting for (**A**) 20-u.c. $Cu_3Co_2SbO_6$ thin film with the $T_N \sim 15.7 \pm 1.6$ K, (**B**) 5-u.c. $Cu_3Co_2SbO_6$ thin film with the $T_N \sim 17.1 \pm 1.3$ K, (**C**) 3-u.c. $Cu_3Co_2SbO_6$ thin film with the $T_N \sim 22.7 \pm 1.8$ K, (**D**) He-implanted $Cu_3Co_2SbO_6$ (1.7×10^{15} cm^{-2}) with the $T_N \sim 12.7 \pm 1.4$ K, (**E**) He-implanted $Cu_3Co_2SbO_6$ (2.6×10^{15} cm^{-2}) with the $T_N \sim 9.3 \pm 1$ K, and (**F**) He-implanted $Cu_3Co_2SbO_6$ (3.6×10^{15} cm^{-2}) with the $T_N \sim 7.8 \pm 1$ K. Almost 90% of modulation in T_N is achieved by in-plane and out-of-plane stretching of $Cu_3Co_2SbO_6$ films. (**G**) The Δ_{trig}-versus-T_N graph clearly visualizes strong positive correlations between those two parameters in the layered cobaltates. The gray dashed line is guided for eyes. Although $Na_3Co_2SbO_6$ has a different space group from $Cu_3Co_2SbO_6$, it follows the same relationship between T_N and Δ_{trig} found in $Cu_3Co_2SbO_6$, as highlighted by a star (fig. S9). Therefore, the Δ_{trig} can be considered the key parameter for destabilizing classical magnetic ground state in the layered honeycomb cobaltates.

At first glance, this result seems to be inconsistent with our experimental observation that a suppression in trigonal distortion decreases T_N. It turns out that the enhanced geometrical frustration induced by the competition between the antiferromagnetic J_3 and the ferromagnetic J_1 under the reduced trigonal distortion explains the observed phenomena. In our layered honeycomb cobaltate system, while large J_3/J_1 prefers the antiferromagnetic zigzag ground state, small J_3/J_1 prefers the ferromagnetic ground state. In between two different regimes, close to $J_3/J_1 \sim -0.3$, geometric frustration dominates, which results in either spin spiral state (*52*) or a spin liquid–like phase when quantum fluctuations are considered (*52, 53*). At the ambient condition, J_3/J_1 is about -1.6, implying the presence of a zigzag-ordered phase (*52, 53*). As the tensile strain along the c axis is applied, J_1 is being enhanced via the suppression of the trigonal distortion, and, as a result, the J_3/J_1 ratio changes from -1.6 at ambient to -1.20 and -0.98 for 1 and 2% of strains, respectively (see table S2 for further information). Hence, the system moves closer to the magnetically frustrated regime ($J_3/J_1 \sim -0.3$) upon the c-axis strain, which should lead to a decrease in T_N (*52–54*).

DISCUSSION
Our findings above have testified to the effectiveness of strain engineering in heterostructures to destabilize unsought long-range ordering in spin liquid candidates. While previous studies in bulk have predominantly focused on the observation of fluctuating spin-disordered phases in response to external magnetic fields (*13, 55–57*), our approach focused on direct manipulation of the spin Hamiltonian parameters. As several theoretical studies have pointed

out (*10, 19, 26, 58*), fine-tuning of spin Hamiltonian seems to be inevitable to realize an otherwise fragile spin liquid state.

We believe that this rather unexplored research direction might provide a route toward realizing elusive quantum phases of matter. On the basis of our experimental and theoretical results, out-of-plane stretched $Cu_3Co_2SbO_6$ heterostructure might approach the QSL regime not by eliminating Heisenberg exchange interactions but by balancing them. With further decreasing trigonal distortion, the exchange interactions J_1 and J_3 can be more balanced, potentially resulting in complete suppression of long-range order. Note that the competition between the J_1 and J_3 Heisenberg interactions has been recently discussed in other Co-based compounds like $BaCo_2(AsO_4)_2$, where the effects of anisotropic magnetic exchange interactions such as Kitaev term are considered marginal so that the XXZ model with small magnetic anisotropy seems a better description (*49, 53*). On the other hand, we emphasize that a sizable Kitaev term in $Cu_3Co_2SbO_6$ can further enhance magnetic frustration closer to the geometrically frustrated regime. In this regime, we speculate that the slightly suppressed but still sizable Kitaev exchange interaction could further stabilize the theoretically proposed spin liquid–like phases and play a major role in realizing novel magnetic phase (*53*). Therefore, theoretical study on such regime will be highly intriguing in layered honeycomb cobaltate system.

Another obvious future research would be identifying substrates and buffer layers that can not only facilitate larger compressive strain but are also potentially applicable to other cobaltates like $Na_3Co_2SbO_6$, which inherently has a smaller trigonal distortion. Limitations in the current study arise from the low volume of ultrathin film and/or helium-induced paramagnetic impurities, which hinder conventional magnetic susceptibility measurement and complicate
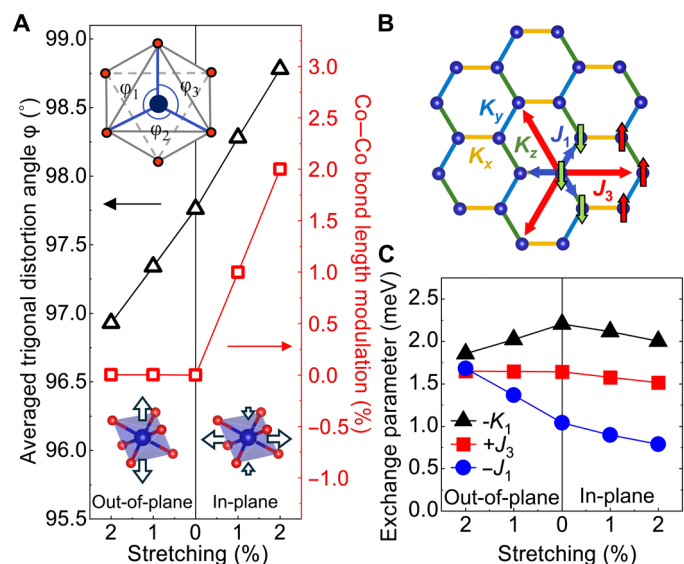
Fig. 6. Magnetic exchange interaction of $Cu_3Co_2SbO_6$ system. (**A**) The averaged trigonal distortion angle, $\varphi = (\varphi_1 + \varphi_2 + \varphi_3)/3$ and Co—Co bond length modulation in stretched $Cu_3Co_2SbO_6$ thin film from ab initio density functional theory + U calculation. In the case of out-of-plane stretching (left side), the in-plane lattice parameter remains fixed to mimic the situation in He ion implantation. (**B**) The dominant magnetic exchange interactions between Co^{2+} ions in $Cu_3Co_2SbO_6$: Kitaev interactions K_x, K_y, and K_z and the ferromagnetic Heisenberg interaction J_1 between nearest-neighbor ions and antiferromagnetic J_3 between third nearest-neighbor ions. The competition between ferromagnetic J_1 and antiferromagnetic J_3 induces a geometrical frustration of magnetic ordering. (**C**) The magnitude of magnetic exchange interactions from first-principles calculations. Increased J_1 would result in larger frustration in the presence of J_3, resulting in suppression of the long-range ordering.

the investigation of antiferromagnetic ordering in Kitaev QSL candidates. In addition, our helium implantation method was found to be not applicable to $Na_3Co_2SbO_6$, as it completely destroyed its crystal structures (fig. S12). While searching for evidence of Kitaev QSL will be notoriously challenging in heterostructures, a few recent theoretical suggestions based on electrical measurement, spintronics, as well as inelastic tunneling experiments can be applicable to our systems (59–62).

In conclusion, we have demonstrated the control of the trigonal distortion of CoO_6 octahedra in $Cu_3Co_2SbO_6$, a promising candidate of Kitaev QSL, and the subsequent destabilization of its classical antiferromagnetic ground state. Our lattice-engineered $Cu_3Co_2SbO_6$ system opens the pathway to tailor the spin interactions in layered honeycomb cobaltate systems, offering valuable insights into the underlying physics of Kitaev materials.

MATERIALS AND METHODS
Sample preparation
The $Na_3Co_2SbO_6$ and $Cu_3Co_2SbO_6$ thin films were synthesized using pulsed laser deposition. For high-quality thin films, the O-faced ZnO [0001] substrates were annealed for 2 hours at 1100°C in ambient pressure. The $Na_3Co_2SbO_6$ and $Cu_3Co_2SbO_6$ targets were synthesized using the solid-state reaction method with the reported recipe of polycrystalline powder (31, 46). The optimized growth

conditions of $Na_3Co_2SbO_6$ were as follows: substrate temperature $T = 625$°C, oxygen partial pressure $P = 1$ mtorr, the energy of the KrF Excimer laser ($\lambda = 248$ nm) $E = 1.1$ J/cm^2, the laser repetition rate is 10 Hz, and the distance between the target and substrate was set at 50 mm. The cooling process was performed under the same as grown pressure after the deposition was completed. For the XAS experiment, 40-u.c. (21-nm) thickness $Na_3Co_2SbO_6$ films were used. For $Cu_3Co_2SbO_6$, optimized growth conditions were a substrate temperature $T = 800$°C, oxygen partial pressure $P = 10$ mtorr, the energy of the KrF Excimer laser ($\lambda = 248$ nm) $E = 1.3$ J/cm^2, laser repetition rate is 10 Hz, and the distance between the target and substrate was set at 50 mm. The cooling process was performed under the same as grown pressure after the deposition was completed. For the helium ion implantation, 20-u.c. (23-nm) thickness $Cu_3Co_2SbO_6$ films were used.

Helium ion implantation
Helium ions were implanted into 20-u.c. $Cu_3Co_2SbO_6$ thin films using a metal ion implanter at in Korea Multi-Purpose Accelerator Complex. Helium ion is injected into each sample with 10-keV energy at room temperature and vacuum environment. Each flux density of helium ion was 1.7×10^{15} cm^{-2}, 2.6×10^{15} cm^{-2}, and 3.6×10^{15} cm^{-2}. To prevent the damage of films due to high-energy ion beam, a 48-nm-thick gold layer was deposited using thermal evaporation. For the XAS measurements, the gold layer was peeled off by Kapton tape. Details about the thickness of the gold layer and average helium ion density in the thin film are determined by Stopping and Range of Ions in Matter/Transport of Ions in Matter Monte Carlo simulation (fig. S13).

Characterization of lattice structure
To characterize the crystal structure of $Cu_3Co_2SbO_6$ thin films, high-resolution XRD data for each $Cu_3Co_2SbO_6$ thin film were collected by using the D8 Advance High-Resolution X-ray Diffractometer (Bruker) with Cu K-α1 wavelength. 0D Lynxeye detector is used in θ-2θ scan, which has 0.01° increment with a scan speed of 0.5 s per step. Each scan has range from 60° to 80° for thickness-dependent $Cu_3Co_2SbO_6$ thin films and from 25° to 40° for helium-implanted thin film. We used the (008) diffraction peak to determine the lattice constant c^* of thickness-controlled $Cu_3Co_2SbO_6$ to avoid overlapping with ZnO substrate peak. For a detailed structural analysis, RSM data of the $Cu_3Co_2SbO_6$ (606) peak and the ZnO (114) peak were conducted on each $Cu_3Co_2SbO_6$ thin film at the 3A Hard X-ray Scattering beamline in PLS-II of the Pohang Accelerator Laboratory.

Cs-corrected STEM
The samples were prepared using a dual-beam focused ion beam (Helios NanoLab 450, FEI) by a Ga-ion beam with 30-kV acceleration voltage. The ADF-STEM images were acquired using Cs-corrected STEM (JEM-ARM200F, JEOL) with 160-kV acceleration voltage. Geometrical phase analysis for the strain mapping is conducted using commercial software DigitalMicrograph3 from GATAN Inc., which is measuring the lattice displacements displayed in ADF-STEM images. Fourier transform of real-space STEM images gives us the displacement of c^* and the a axis. The strain fields of He-implanted $Cu_3Co_2SbO_6$ film (5.1×10^{15} cm^{-2}), ε_{xx} and ε_{yy}, are generated, and uniformities of the layer are confirmed by analyzing the contrast of color map and intensity profile of each strain fields.

X-ray absorption spectroscopy

The XAS measurements were conducted at the 2A Magnetic Spectroscopy beamline in PLS-II of the Pohang Accelerator Laboratory. Those were performed in a zero-applied magnetic field, in a vacuum with a pressure lower than 2×10^{-9} torr at room temperature, and in total electron yield mode. To prevent the charging effect, we bridged four edges of film surfaces and a copper holder with silver paint. Because the implanted helium ions can escape from the samples in high temperature (35), the sample temperature was maintained at room temperature with nitrogen gas during the vacuum baking process. We acquired XAS spectra at the Co L edges and O K edge with an energy resolution of 0.1 and 0.2 eV, respectively. To compare the XAS spectra of different films, they are normalized on the basis of the total area of the isotropic spectra in the range of 770 to 790 eV for Co L_3 edge and of 785 to 805 eV for Co L_2 edge. The absolute area of XLD, $I_{|XLD|}$, is determined by integrating within the range of 775 to 785 eV for Co L_3 edge in XLD spectra. Additional XAS data for each thickness-controlled and helium ion–implanted $Cu_3Co_2SbO_6$ thin films are shown in the Supplementary Materials (figs. S14 to S17).

Crystal field multiplet calculation for Co L-edge XAS

The crystal field multiplet calculations were conducted using the quantum many-body script language, Quanty (39). The user interface called Crispy is used to generate input files consisting of Slater-Condon and crystal field parameters and to visualize the simulated spectra of I_{iso} and I_{XLD} (40). With C_{3v} site symmetry, the crystal field parameters Dq, D_σ, and D_τ were estimated by simulating the experimental L_3-edge spectra. Note that both D_{3d} and C_{3v} have the same trigonal symmetry. The Slater-Condon parameters for electron-electron repulsion (F^k_{dd}, F^k_{pd}) and exchange (G^k_{pd}, G^k_{dd}) were scaled down by multiplying a factor of 80% to compensate for the electronic delocalization in 3d orbital (37). The spin-orbit coupling parameters of 2p and 3d are evaluated as 9.745 and 0.066 eV, respectively. To reproduce the exact shape of each spectrum, 0.4-eV Gaussian broadening is adopted. The Lorentzian broadening for L_2 edge and L_3 edge are selected as 0.5 and 0.6 eV, respectively.

Ellipsometry

We measured the ellipsometry parameters Ψ and Δ of $Cu_3Co_2SbO_6$ thin films on ZnO substrate by using an M-2000 ellipsometer (J.A. Woollam Co.). $\tan\Psi$ is the amplitude ratio of the reflected p- and s-waves, while Δ represents the phase shift between the two waves. For all samples, Ψ and Δ were obtained across an energy range from 0.74 to 6.46 eV (5900 to 52,000 cm^{-1}) at an incident angle of 60° (80° for 3-u.c. $Cu_3Co_2SbO_6$ for adapting good sensitivity) and over a temperature range of 6 to 300 K. Each data collection lasted 200 s. For low-T measurement, the window effect was calibrated by using a 25-nm SiO_2/Si wafer. To prevent degradation of the sample implanted helium ions, we avoided baking out the chamber. The base pressure has remained below 1×10^{-8} torr. All samples were mounted using carbon tape to oxygen-free copper cones.

Magnetic susceptibility

Field-cooled magnetization curves with respect to the temperature for $Cu_3Co_2SbO_6$, $Na_3Co_2SbO_6$, and He-implanted $Cu_3Co_2SbO_6$ thin films on ZnO substrate were measured by superconducting quantum interference device (Quantum Design). The mass and dimension of each sample were precisely investigated as 13.6 mg and 3.3 mm by 2.5 mm. We measured magnetization with the direction of ZnO (110). Also, to compensate paramagnetic signal from the substrate, the magnetization of ZnO with the same dimension of 13.6 mg was obtained. During measurements, samples are attached to a quartz plate mounted by GE varnish. All magnetic susceptibility data were calculated by substituting the diamagnetic signal in the substrate with mass-normalization.

First-principles calculation of magnetic exchange interactions

Vienna Ab initio Simulation Package was used for the computation of the electronic structure of $Cu_3Co_2SbO_6$ (63). Electronic structure calculations and optimizations of the crystal structure were performed using a revised Perdew-Burke-Ernzerhof generalized gradient approximation for solids (64). In addition, for the reasonable description of structural properties under strain, an effective on-site Coulomb repulsion parameter $U_{eff} = 4$ eV within the cobalt d-orbitals was incorporated via a rotationally invariant flavor of density functional theory $+ U$ formalism (65). We turned on both a Néel-type antiferromagnetic order and $U_{eff} = 4$ eV during the optimizations of crystal structure under strain. The primitive Brillouin zone of $Cu_3Co_2SbO_6$ was sampled with an $8 \times 8 \times 4$ Monkhorst-Pack k-mesh, and the plane wave cutoff was fixed to 500 eV. The force and energy tolerance factors were set to 10^{-4} eV/Å and 10^{-9} eV, respectively. To compute hopping integrals between Co d- and O p-orbitals, the maximally localized Wannier function method (66) as implemented in Wannier90 (67) was used. For the estimation of spin Hamiltonian parameters, we used the perturbative expression given in (50).

For the simulation of strain effects, we used two structural models. In the case with the out-of-plane stretch, we increased the c-axis parameters while fixing the in-plane parameter, assuming that the in-plane parameters remain fixed due to the epitaxial strain. In the situation with the in-plane stretch, we tuned the in-plane lattice parameters in an isotropic manner while the c-axis parameter relaxed. In both cases, internal atomic coordinates were fully relaxed (see tables S1 and S2).

Supplementary Materials

This PDF file includes:
Supplementary Text
Figs. S1 to S17
Tables S1 and S2

REFERENCES AND NOTES

1. P. W. Anderson, Resonating valence bonds: A new kind of insulator? *Mater. Res. Bull.* **8**, 153–160 (1973).
2. P. W. Anderson, G. Baskaran, Z. Zou, T. Hsu, Resonating–valence-bond theory of phase transitions and superconductivity in La_2CuO_4-based compounds. *Phys. Rev. Lett.* **58**, 2790–2793 (1987).
3. Y. Zhou, K. Kanoda, T.-K. Ng, Quantum spin liquid states. *Rev. Mod. Phys.* **89**, 025003 (2017).
4. C. Broholm, R. J. Cava, S. A. Kivelson, D. G. Nocera, M. R. Norman, T. Senthil, Quantum spin liquids. *Science* **367**, eaay0668 (2020).
5. A. Kitaev, Anyons in an exactly solved model and beyond. *Ann. Phys. Rehabil. Med.* **321**, 2–111 (2006).
6. J. Chaloupka, G. Jackeli, G. Khaliullin, Kitaev-Heisenberg model on a honeycomb lattice: Possible exotic phases in iridium oxides A_2IrO_3. *Phys. Rev. Lett.* **105**, 027204 (2010).
7. Y. Singh, S. Manni, J. Reuther, T. Berlijn, R. Thomale, W. Ku, S. Trebst, P. Gegenwart, Relevance of the Heisenberg-Kitaev model for the honeycomb lattice iridates A_2IrO_3. *Phys. Rev. Lett.* **108**, 127203 (2012).
8. H. Gretarsson, J. P. Clancy, X. Liu, J. P. Hill, E. Bozin, Y. Singh, S. Manni, P. Gegenwart, J. Kim, A. H. Said, D. Casa, T. Gog, M. H. Upton, J. Y. Heung-Sik Kim, V. M. Katukuri, L. Hozoi,

J. van den Brink, Y.-J. Kim, Crystal-field splitting and correlation effect on the electronic structure of A$_2$IrO$_3$. *Phys. Rev. Lett.* **110**, 076402 (2013).

9. M. Jenderka, J. Barzola-Quiquia, Z. Zhang, H. Frenzel, M. Grundmann, M. Lorenz, Mott variable-range hopping and weak antilocalization effect in heteroepitaxial Na$_2$IrO$_3$ thin films. *Phys. Rev. B* **88**, 045111 (2013).

10. Y. Yamaji, T. Suzuki, T. Yamada, S.-I. Suga, N. Kawashima, M. Imada, Clues and criteria for designing a Kitaev spin liquid revealed by thermal and spin excitations of the honeycomb iridate Na$_2$IrO$_3$. *Phys. Rev. B* **93**, 174425 (2016).

11. R. D. Johnson, S. C. Williams, A. A. Haghighirad, J. Singleton, V. Zapf, P. Manuel, I. I. Mazin, Y. Li, H. O. Jeschke, R. Valentí, Monoclinic crystal structure of α-RuCl$_3$ and the zigzag antiferromagnetic ground state. *Phys. Rev. B* **92**, 235119 (2015).

12. M. Majumder, M. Schmidt, H. Rosner, A. Tsirlin, H. Yasuoka, M. Baenitz, Anisotropic Ru^{3+} 4d^5 magnetism in the α−RuCl$_3$ honeycomb system: Susceptibility, specific heat, and zero-field NMR. *Phys. Rev. B* **91**, 180401 (2015).

13. S.-H. Baek, S.-H. Do, K.-Y. Choi, Y. S. Kwon, A. U. B. Wolter, S. Nishimoto, J. van den Brink, B. Büchner, Evidence for a field-induced quantum spin liquid in α-RuCl$_3$. *Phys. Rev. Lett.* **119**, 037201 (2017).

14. A. Banerjee, J. Yan, J. Knolle, C. A. Bridges, M. B. Stone, M. D. Lumsden, D. G. Mandrus, D. A. Tennant, R. Moessner, S. E. Nagler, Neutron scattering in the proximate quantum spin liquid α-RuCl$_3$. *Science* **356**, 1055–1059 (2017).

15. S.-H. Do, S.-Y. Park, J. Yoshitake, J. Nasu, Y. Motome, Y. S. Kwon, D. T. Adroja, D. J. Voneshen, K. Kim, T. H. Jang, J. H. Park, K.-Y. Choi, S. Ji, Majorana fermions in the Kitaev quantum spin system α-RuCl$_3$. *Nat. Phys.* **13**, 1079–1084 (2017).

16. H. Liu, J. Chaloupka, G. Khaliullin, Exchange interactions in d^5 Kitaev materials: From Na$_2$IrO$_3$ to α−RuCl$_3$. *Phys. Rev. B* **105**, 214411 (2022).

17. T. Yokoi, S. Ma, Y. Kasahara, S. Kasahara, T. Shibauchi, N. Kurita, H. Tanaka, J. Nasu, Y. Motome, C. Hickey, S. Trebst, Y. Matsuda, Half-integer quantized anomalous thermal Hall effect in the Kitaev material candidate α-RuCl$_3$. *Science* **373**, 568–572 (2021).

18. R. Sano, Y. Kato, Y. Motome, Kitaev-Heisenberg Hamiltonian for high-spin d^7 Mott insulators. *Phys. Rev. B* **97**, 014408 (2018).

19. H. Liu, Towards Kitaev spin liquid in 3d transition metal compounds. *Int. J. Mod. Phys B* **35**, 2130006 (2021).

20. G. Jackeli, G. Khaliullin, Mott insulators in the strong spin-orbit coupling limit: From Heisenberg to a quantum compass and Kitaev models. *Phys. Rev. Lett.* **102**, 017205 (2009).

21. H. Liu, G. Khaliullin, Pseudospin exchange interactions in d^7 cobalt compounds: Possible realization of the Kitaev model. *Phys. Rev. B* **97**, 014407 (2018).

22. H. Liu, J. Chaloupka, G. Khaliullin, Kitaev spin liquid in 3d transition metal compounds. *Phys. Rev. Lett.* **125**, 047201 (2020).

23. E. Lefrançois, M. Songvilay, J. Robert, G. Nataf, E. Jordan, L. Chaix, C. Colin, P. Lejay, A. Hadj-Azzem, R. Ballou, Magnetic properties of the honeycomb oxide Na$_2$Co$_2$TeO$_6$. *Phys. Rev. B* **94**, 214416 (2016).

24. M. Songvilay, J. Robert, S. Petit, J. A. Rodriguez-Rivera, W. D. Ratcliff, F. Damay, V. Balédent, M. Jiménez-Ruiz, P. Lejay, E. Pachoud, Kitaev interactions in the Co honeycomb antiferromagnets Na$_3$Co$_2$SbO$_6$ and Na$_2$Co$_2$TeO$_6$. *Phys. Rev. B* **102**, 224429 (2020).

25. X. Li, Y. Gu, Y. Chen, V. O. Garlea, K. Iida, K. Kamazawa, Y. Li, G. Deng, Q. Xiao, X. Zheng, Giant magnetic in-plane anisotropy and competing instabilities in Na$_3$Co$_2$SbO$_6$. *Phys. Rev. X* **12**, 041024 (2022).

26. A. L. Sanders, R. A. Mole, J. Liu, A. J. Brown, D. Yu, C. D. Ling, S. Rachel, Dominant Kitaev interactions in the honeycomb materials Na$_3$Co$_2$SbO$_6$ and Na$_2$Co$_2$TeO$_6$. *Phys. Rev. B* **106**, 014413 (2022).

27. E. Vavilova, T. Vasilchikova, A. Vasiliev, D. Mikhailova, V. Nalbandyan, E. Zvereva, S. V. Streltsov, Magnetic phase diagram and possible Kitaev-like behavior of the honeycomb-lattice antimonate Na$_3$Co$_2$SbO$_6$. *Phys. Rev. B* **107**, 054411 (2023).

28. X. Zhang, Y. Xu, T. Halloran, R. Zhong, C. Broholm, R. J. Cava, N. P. Drichko, N. Armitage, A magnetic continuum in the cobalt-based honeycomb magnet BaCo$_2$(AsO$_4$)$_2$. *Nat. Mater.* **22**, 58–63 (2023).

29. R. Zhong, T. Gao, N. P. Ong, R. J. Cava, Weak-field induced nonmagnetic state in a Co-based honeycomb. *Sci. Adv.* **6**, eaay6953 (2020).

30. J.-Q. Yan, S. Okamoto, Y. Wu, Q. Zheng, H. D. Zhou, H. B. Cao, M. A. McGuire, Magnetic order in single crystals of Na$_3$Co$_2$SbO$_6$ with a honeycomb arrangement of 3d^7 Co^{2+} ions. *Phys. Rev. Materials* **3**, 074405 (2019).

31. J. H. Roudebush, N. H. Andersen, R. Ramlau, V. O. Garlea, R. Toft-Petersen, P. Norby, R. Schneider, J. N. Hay, R. J. Cava, Structure and magnetic properties of Cu$_3$Ni$_2$SbO$_6$ and Cu$_3$Co$_2$SbO$_6$ delafossites with honeycomb lattices. *Inorg. Chem.* **52**, 6083–6095 (2013).

32. B. Kang, U. Choi, T. S. Jung, S. Noh, G.-H. Kim, U. Seo, M. Park, J.-H. Choi, M. Kim, G. Ji, Optical detection of bond-dependent and frustrated spin in the two-dimensional cobalt-based honeycomb antiferromagnet Cu$_3$Co$_2$SbO$_6$. arXiv:2309.15753 (2023).

33. J. Chakhalian, J. M. Rondinelli, J. Liu, B. A. Gray, M. Kareev, E. J. Moon, N. Prasai, J. L. Cohn, M. Varela, I. C. Tung, M. J. Bedzyk, S. G. Altendorf, F. Strigari, B. Dabrowski, L. H. Tjeng, P. J. Ryan, J. W. Freeland, Asymmetric orbital-lattice interactions in ultrathin correlated oxide films. *Phys. Rev. Lett.* **107**, 116805 (2011).

34. H. Guo, S. Dong, P. D. Rack, J. D. Budai, C. Beekman, Z. Gai, W. Siemons, C. Gonzalez, R. Timilsina, A. T. Wong, Strain doping: Reversible single-axis control of a complex oxide lattice via helium implantation. *Phys. Rev. Lett.* **114**, 256801 (2015).

35. M. Brahlek, A. R. Mazza, A. Annaberdiyev, M. Chilcote, G. Rimal, G. B. Halász, A. Pham, Y.-Y. Pai, J. T. Krogel, J. Lapano, Emergent magnetism with continuous control in the ultrahigh-conductivity layered oxide PdCoO$_2$. *Nano Lett.* **23**, 7279–7287 (2023).

36. M. van Veenendaal, E. Poldi, L. Veiga, P. Bencok, G. Fabbris, R. Tartaglia, J. McChesney, J. W. Freeland, H. Remley, H. Zheng, Electronic structure of Co 3d states in the Kitaev material candidate honeycomb cobaltate Na$_3$Co$_2$SbO$_6$ probed with x-ray dichroism. *Phys. Rev. B* **107**, 214443 (2023).

37. M. M. van Schooneveld, R. Kurian, A. Juhin, K. Zhou, J. Schlappa, V. N. Strocov, T. Schmitt, F. M. F. de Groot, Electronic structure of CoO nanocrystals and a single crystal probed by resonant x-ray emission spectroscopy. *J. Phys. Chem. C* **116**, 15218–15230 (2012).

38. F. Y. Bruno, K. Z. Rushchanskii, S. Valencia, Y. Dumont, C. Carrétéro, E. Jacquet, R. Abrudan, S. Blügel, M. Ležaić, M. Bibes, A. Barthélémy, Rationalizing strain engineering effects in rare-earth nickelates. *Phys. Rev. B* **88**, 195108 (2013).

39. M. W. Haverkort, M. Zwierzycki, O. K. Andersen, Multiplet ligand-field theory using Wannier orbitals. *Phys. Rev. B* **85**, 165113 (2012).

40. M. Retegan, Crispy, version 0.7.3, Zenodo (2019); https://doi.org/10.5281/zenodo.3258065.

41. F. de Groot, M. Grioni, J. C. Fuggle, J. Ghijsen, G. A. Sawatzky, H. Petersen, Oxygen is x-ray-absorption edges of transition-metal oxides. *Phys. Rev. B* **40**, 5715–5723 (1989).

42. M. Grioni, J. F. van Acker, M. T. Czyzyk, J. C. Fuggle, Unoccupied electronic structure and core-hole effects in the x-ray absorption spectra of Cu$_2$O. *Phys. Rev. B: Condens. Matter* **45**, 3309–3318 (1992).

43. A. B. Gurevich, B. E. Bent, A. V. Teplyakov, J. G. Chen, A NEXAFS investigation of the formation and decomposition of CuO and Cu$_2$O thin films on Cu (100). *Surf. Sci.* **442**, L971–L976 (1999).

44. W. B. Wu, D. J. Huang, J. Okamoto, A. Tanaka, H. J. Lin, F. C. Chou, A. Fujimori, C. T. Chen, Orbital symmetry and electron correlation in Na$_x$CoO$_2$. *Phys. Rev. Lett.* **94**, 146402 (2005).

45. B. Kang, M. Park, S. Song, S. Noh, D. Choe, M. Kong, M. Kim, C. Seo, E. K. Ko, G. Yi, Honeycomb oxide heterostructure as a candidate host for a Kitaev quantum spin liquid. *Phys. Rev. B* **107**, 075103 (2023).

46. C. Wong, M. Avdeev, C. D. Ling, Zig-zag magnetic ordering in honeycomb-layered Na$_3$Co$_2$SbO$_6$. *J. Solid State Chem.* **243**, 18–22 (2016).

47. G. Lin, J. Jeong, C. Kim, Y. Wang, Q. Huang, T. Masuda, S. Asai, S. Itoh, G. Günther, M. Russina, Field-induced quantum spin disordered state in spin-1/2 honeycomb magnet Na$_2$Co$_2$TeO$_6$. *Nat. Commun.* **12**, 5559 (2021).

48. S. M. Winter, Magnetic couplings in edge-sharing high-spin d^7 compounds. *J. Phys. Mater.* **5**, 045003 (2022).

49. T. Halloran, F. Desrochers, E. Z. Zhang, T. Chen, L. E. Chern, Z. Xu, B. Winn, M. Graves-Brook, M. Stone, A. I. Kolesnikov, Geometrical frustration versus Kitaev interactions in BaCo$_2$(AsO$_4$)$_2$. *Proc. Natl. Acad. Sci. U.S.A.* **120**, e2215509119 (2023).

50. X. Liu, H.-Y. Kee, Non-Kitaev versus Kitaev honeycomb cobaltates. *Phys. Rev. B* **107**, 054420 (2023).

51. P. A. Maksimov, A. V. Ushakov, Z. V. Pchelkina, Y. Li, S. M. Winter, S. V. Streltsov, Ab initio guided minimal model for the "Kitaev" material BaCo$_2$(AsO$_4$)$_2$: Importance of direct hopping, third-neighbor exchange, and quantum fluctuations. *Phys. Rev. B* **106**, 165131 (2022).

52. J. B. Fouet, P. Sindzingre, C. Lhuillier, An investigation of the quantum J_1-J_2-J_3 model on the honeycomb lattice. *Eur. Phys. J. B* **20**, 241–254 (2001).

53. A. Bose, M. Routh, S. Voleti, S. K. Saha, M. Kumar, T. Saha-Dasgupta, A. Paramekanti, Proximate Dirac spin liquid in the honeycomb lattice J_1-J_3 model: Numerical study and application to cobaltates. *Phys. Rev. B* **108**, 174422 (2023).

54. E. Rastelli, A. Tassi, L. Reatto, Non-simple magnetic order for simple Hamiltonians. *Physica B+C* **97**, 1–24 (1979).

55. Z. Wang, S. Reschke, D. Hüvonen, S.-H. Do, K.-Y. Choi, M. Gensch, U. Nagel, T. Rõõm, A. Loidl, Magnetic excitations and continuum of a possibly field-induced quantum spin liquid in α-RuCl$_3$. *Phys. Rev. Lett.* **119**, 227202 (2017).

56. J. Zheng, K. Ran, T. Li, J. Wang, P. Wang, B. Liu, Z.-X. Liu, B. Normand, J. Wen, W. Yu, Gapless spin excitations in the field-induced quantum spin liquid phase of α-RuCl$_3$. *Phys. Rev. Lett.* **119**, 227208 (2017).

57. Y.-F. Jiang, T. P. Devereaux, H.-C. Jiang, Field-induced quantum spin liquid in the Kitaev-Heisenberg model and its relation to α-RuCl$_3$. *Phys. Rev. B* **100**, 165123 (2019).

58. S. M. Winter, Y. Li, H. O. Jeschke, R. Valentí, Challenges in design of Kitaev materials: Magnetic interactions from competing energy scales. *Phys. Rev. B* **93**, 214431 (2016).

59. J. Aftergood, S. Takei, Probing quantum spin liquids in equilibrium using the inverse spin Hall effect. *Phys. Rev. Res.* **2**, 033439 (2020).

60. E. J. König, M. T. Randeria, B. Jäck, Tunneling spectroscopy of quantum spin liquids. *Phys. Rev. Lett.* **125**, 267206 (2020).

61. T. Minakawa, Y. Murakami, A. Koga, J. Nasu, Majorana-mediated spin transport in Kitaev quantum spin liquids. *Phys. Rev. Lett.* **125**, 047204 (2020).

62. R. G. Pereira, R. Egger, Electrical access to ising anyons in kitaev spin liquids. *Phys. Rev. Lett.* **125**, 227202 (2020).

63. G. Kresse, J. Furthmüller, Efficient iterative schemes for *ab initio* total-energy calculations using a plane-wave basis set. *Phys. Rev. B* **54**, 11169–11186 (1996).

64. J. P. Perdew, A. Ruzsinszky, G. I. Csonka, O. A. Vydrov, G. E. Scuseria, L. A. Constantin, X. Zhou, K. Burke, Restoring the density-gradient expansion for exchange in solids and surfaces. *Phys. Rev. Lett.* **100**, 136406 (2008).

65. S. L. Dudarev, G. A. Botton, S. Y. Savrasov, C. Humphreys, A. P. Sutton, Electron-energy-loss spectra and the structural stability of nickel oxide: An LSDA+U sudy. *Phys. Rev. B* **57**, 1505–1509 (1998).

66. I. Souza, N. Marzari, D. Vanderbilt, Maximally localized Wannier functions for entangled energy bands. *Phys. Rev. B* **65**, 035109 (2001).

67. G. Pizzi, V. Vitale, R. Arita, S. Blügel, F. Freimuth, G. Géranton, M. Gibertini, D. Gresch, C. Johnson, T. Koretsune, Wannier90 as a community code: New features and applications. *J. Phys. Condens. Matter* **32**, 165902 (2020).